Multi-frequency differential absorption lidar incorporating a comb-referenced scanning laser for gas spectrum analysis

SAIFEN YU,[1] ZHEN ZHANG,[1] MANYI LI,[1] AND HAIYUN XIA[1,2,3,*]

[1]*CAS Key Laboratory of Geospace Environment, School of Earth and Space Science, USTC, Hefei 230026, China*
[2]*Hefei National Laboratory for Physical Sciences at the Microscale, Hefei 230026, China*
[3]*CAS Center for Excellence in Comparative Planetology, Hefei, 230026, China*
[*]hsia@ustc.edu.cn

Abstract: A multi-frequency differential absorption lidar incorporating a tunable laser and an optical frequency comb is demonstrated for precise spectrum analysis of atmospheric gas. The single frequency tunable laser is stabilized by locking to the optical frequency comb, with a standard deviation of 0.5 MHz. To achieve a high signal-to-noise ratio, a multi-mode superconducting nanowire single-photon detector with an active-area diameter of 50 μm, a quantum efficiency of 31.5%, and dark noise of 100 counts per second is implemented, which enables to avoid the need for high energy lasers. In the experiment, the range-resolved spectrum of atmospheric mixture gases (CO_2 and HDO) in a region of 1572.2 - 1572.45 nm is obtained. Results show different partially overlapped absorption of two gases in different seasons, with a stronger influence of HDO on CO_2 in summer than in winter. The interactions are taken into account by separating the mixture absorption spectrum (one CO_2 line and two HDO lines) with triple-peak Voigt fitting. The retrieved concentrations over 6 km with a range resolution of 120 m and a time resolution of 10 min are compared with in-situ sensors. The uncertainties of the retrieved concentrations are as low as 6.5 μmol/mol (ppm) and 1×10^{-3} g/kg for CO_2 and HDO, respectively.

1. Introduction

Long-lived greenhouse gases (GHGs) absorb the longwave radiation coming from the surface, affecting the radiation balance of the Earth [1]. Since the start of the industrial era, GHGs increases are greatly attributed to human activities [2]. Carbon dioxide (CO_2) and methane (CH_4) are the most potent GHGs after water vapor, such gases together with nitrous oxide (N_2O) and ozone (O_3) related trace gases accumulate in the atmosphere thus warm the global climate, causing extreme events, glaciers melting and sea level rising [3]. It is extremely important to predict and determine the sources and sinks of these gases in the atmosphere [4,5]. In the past decades, passive and active methods have been used to track and quantify atmospheric transport and mixing of gases. The methods based on passive spectrometers [6,7] relying on sunlight are not applicable at night. While the light detection and range (lidar) is widely applied in atmospheric remote sensing for its active light source [8]. The most common differential absorption lidar (DIAL) and integrated path differential absorption (IPDA) lidar use two wavelengths. The offline wavelength is selected at a close-by region of the absorption line with negligible gas absorption, while the online wavelength is set close to a maximum of absorption [9]. These methods have been proposed to remotely sense the atmospheric gases in ground, airborne and space-borne platforms [9–15].

Gas absorption spectrum analysis is important for atmospheric chemistry and physics research, since spectrum results from not only gas concentration but also pressure and temperature of

the atmosphere. Multi-frequency DIAL and IPDA [11,16–19] are effective ways to obtain the broadband gas absorption spectrum for gas remote sensing. The reported light sources include multiple fixed-wavelength distributed-feedback laser diodes (DFB-LDs) [16], scanning DFB monitored by heterodyne detection [17], and injection-seeding optical parametric oscillator (OPO) [18]. With the development of frequency comb [20,21] with evenly-spaced optical modes, new opportunities are opened up for spectrum analysis methods and frequency locking systems. Dual-frequency combs have been field-deployed to monitor GHGs in open paths [22–25]. Meanwhile, a tunable laser can be locked to the comb with an absolute frequency through phase locking [26] and injection locking [27] system.

Here, an all-fiber multi-frequency DIAL incorporating a comb-referenced scanning laser is demonstrated to analyze the spectrum of CO_2 and HDO (isotopic water vapor) in the wavelength range of 1572.22 - 1572.45 nm. The optical frequency comb is contributed to realize frequency locking and mode-hop-free tuning of the tunable laser with a simple feedback loop, which restrains the frequency uncertainty (standard deviation) less than 0.5 MHz during 120 s integration time. The backscatter signal is detected by a multi-mode fiber (MMF) coupled superconducting nanowire single-photon detector (SNSPD), which provides high coupling efficiency. In the experiment, the mixed spectrum of one CO_2 line and two HDO lines are obtained by using a 400 ns pulse with energy of 40 μJ, where the range and time resolutions are 120 m and 10 min, respectively. The three absorption lines are separated by triple-peak Voigt fitting and the independent CO_2 spectra influenced by the concentration of HDO in dry (winter) and moist (summer) environments are analyzed. The lidar system has the potential to monitor GHGs in ground-based or flight-based platforms.

The paper is organized as follows. In Section 2, the optical layout and system parameters are introduced. Section 3 contains two subsections. In Subsection 3.1, the frequency tuning and locking method using comb-referenced subsystem is presented. In Subsection 3.2, the experiment of range-resolved spectrum analysis in different seasons is performed and the concentration results are discussed. A summary with conclusions is provided in Section 4.

2. System description

The optical layout of the system involves frequency locking channel, emission channel, and receiving channel, as shown in Fig. 1. In the frequency locking channel, a home-made frequency comb is used to calibrate the frequency of the external-cavity diode lasers (ECDL). The repetition frequency and the carrier-envelope offset frequency of the comb are $f_r = 100$ MHz and $f_{ceo} = 20$ MHz respectively. Both f_r and f_{ceo} are phase locked to a microwave rubidium clock. The signal of f_r is mixed with a reference and the output of the mixer is feedback to a piezo-electric transducer (PZT) which changes the cavity length of the laser oscillator for tuning the repetition frequency. The frequency stability of f_r measured as the Allan deviation reach 5×10^{-12} and 8.5×10^{-14} at an integration time of 1 s and 1000 s, respectively. The carrier-envelope offset frequency f_{ceo} is generated from a nonlinear $f - 2f$ interferometer [28] with octave-spanning spectrum generation. The locking scheme for f_{ceo} is the same as that for f_r, except that the error signal is feedback to the current of the pump diode of the laser oscillator. The frequency stability of f_{ceo} reaches 1.2×10^{-9} and 2.4×10^{-11} at an integration time of 1 s and 1000 s, respectively. The ECDL (Toptica CTL 1550) covering 1530 ~ 1620 nm is served as a seed laser, and 1% part of the output light is combined with the comb to perform heterodyne detection. The beat frequency enters a balanced detector (BD) and is further filtered by a low pass filter (LPF) to restrain the beat frequency within 48 MHz. Then, the beat frequency is read by a frequency counter. By performing a feedback locking loop based on the beat frequency, the optical frequency of the seed laser can be locked to any preset value.

The emission channel utilizes the 99% part of the seed laser. The seed laser is chopped into a pulse train by using an acoustic optical modulator (AOM) with a pulse repetition of 20 kHz
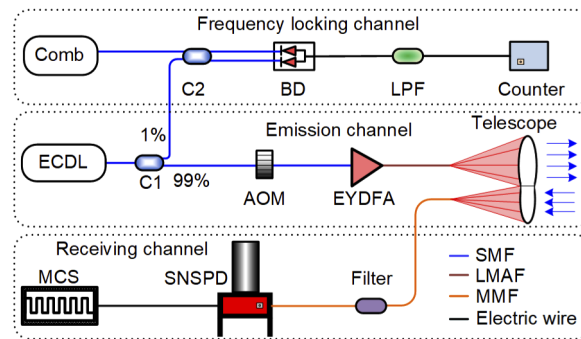
Fig. 1. Optical layout of the frequency locked lidar for multi-gas measurement. BD: balanced detector; LPF, low pass filter; AOM, acoustic optical modulator; EYDFA: erbium-doped and ytterbium-doped fiber amplifier; SNSPD: superconducting nanowire single-photon detector; MCS: multi-channel scaler; SMF: single-mode fiber; LMAF: large-mode-area fiber, MMF: multi-mode fiber.

and a pulse width of 400 ns. Then the energy of laser pulse is amplified to 40 μJ by using an erbium-doped and ytterbium-doped fiber amplifier (EYDFA, Leisheng EYDFA) with an output fiber diameter of 20 μm and numerical aperture of 0.08. The amplified laser pulses are collimated and sent to the atmosphere through a collimator with a diameter of 100 mm and a divergence angle of 40 μrad. Then, the pulses with different wavelengths go through varying degrees of gas absorption, which is stronger near the line center and weaker along the two sides.

In the receiving channel, the backscatter signals from the atmosphere are coupled into MMF with a core diameter of 50 μm and numerical aperture of 0.22 through a telescope with a diameter of 256 mm and a field of view (FOV) of 90 μrad. A flattop filter (Optizone, MMF1572) centered at 1572.335 nm with bandwidth of ±0.15 nm and a peak transmission of 85% is mounted outside the Dewar of the SNSPD to suppress the solar background noise, so that daytime measurement can be realized. Considering the influence of the atmospheric turbulence, an SNSPD with large active diameter of 50 μm is manufactured instead of using the commercially available SNSPD coupled with single-mode fiber (active diameter of 9 μm) [29]. The SNSPD is operated in a 2.2-K compact Gifford–McMahon (G-M) cryocooler. To improve the maximum count rates of the detector, the large active area is divided into 9 pixels and each pixel consists of serially connected two superconducting nanowire avalanche photodetectors (SC-2SNAP) [30]. The SNSPD array is biased and read out by nine homemade electrical modules, the amplified output signals are fed to a multi-channel scaler. The measured total system detection efficiency of our SNSPD array is 31.5% at 1572 nm, and the system dark count rate (DCR) is 100 counts per second. Due to the multi-pixel layout and SC-2SNAP structure, the maximum count rate of the detector is above 30 MHz. Here, low DCR of the MMF coupled SNSPD is realized by using optical filter inside the G-M cryocooler [31], achieving a low noise equivalent power of about 5.7×10^{-18} W/Hz$^{1/2}$ [32].

An overview of the system parameters compared to the reported works is given in Table 1. Usually, the injection-seed OPOs are used [9,18,33] to amplify the pulse energy to a certain value for high SNR, with a limited frequency tuning range of the laser. In this work, the pulse energy is amplified by an EYDFA conveniently. The multi-IPDA technique retrieves path integral gas concentration, which lacks range resolution. While the multi-DIAL technique retrieves range-resolved spectra along the optical path. Here, an optical frequency comb is used to stabilize the frequency of tunable laser with an improved frequency uncertainty. A multi-mode SNSPD with high quantum efficiency and lower dark noise is applied to achieve high SNR.

Table 1. Overview of the system parameters.[a]

Parameters	IPDA		DIAL		
	2-λ [9]	N-λ [11,17,34]	2-λ [33]	N-λ [18]	N-λ [This work]
N	2	15 or 30	2	10	30
Wavelength range (nm)	on: 1572.020 off: 1572.120	1572.235 - 1572.440	on: 2050.972 off: 2050.888	1602.039 - 1602.360	1572.220 - 1572.450
PRF	50 Hz	10 kHz	30 Hz	100 Hz	20 kHz
Pulse energy	10 mJ	25 μJ	5–10 mJ	7 mJ	40 μJ
Pulse width	20 ns	1 μs	10 ns	3 ns	400 ns
Frequency uncertainty	/	1 MHz	/	20 MHz	0.5 MHz
Telescope diameter	60 & 200 mm	200 mm	254 mm	258 mm	256 mm
Bandpass filter	/	0.7 nm flattop, T>95%	/	2 nm FWHM T>90%	0.3 nm flattop, T>85%
Detector type	APD & PIN	HgCdTe APD	InGaAs PIN	InGaAs PMT	SNSPD
Quantum efficiency	10%	70%	10%	3% - 8%	31.5%
Dark count (per second)	/	2.2×10^6	/	2.5×10^5	100
NEP ($W/Hz^{1/2}$)	/	0.5×10^{-15}	3.0×10^{-12}	/	5.7×10^{-18}
CO_2 precision	0.5%	0.2%	10%	1.5%	1.5%
Time resolution	1 s	1 s	9 min	10 min	10 min
Range resolution	N/A	N/A	150 m	250 m	120 m
Orientation	Vertical	Vertical	Tilt 45°	Tilt 18.4°	Horizontal
Distance	20 km (aircraft altitude)	13 km (aircraft altitude)	1 km	5.5 km	6 km

[a]The detection methods of all systems are direct detection. N: number of the sampling wavelength; PRF: pulse repetition frequency; T: peak transmission; PMT: photomultiplier tubes; APD: avalanche photodiodes; PIN: positive intrinsic-negative; NEP: noise equivalent power; /: not mentioned; N/A: not available.

3. Experiment

3.1. Frequency tuning and locking

Figure 2 shows the principle of the frequency tuning and locking process. For atmospheric CO_2 spectrum scanning, the frequency span of the seed laser is adapted to its absorption cross-section in Fig. 2(a). The seed laser beats with an optical frequency comb with uniform spaced optical lines. As shown in Fig. 2(b), the beat frequency f_b depends on the difference frequency between the seed laser and the nearest n^{th} comb tooth, where the frequency is $f_n = n \cdot f_r + f_{ceo}$ ($n = 1$, 2, 3...). The corresponding specific optical frequency of the seed laser can be described as $f_e = f_n \pm f_b$, which is tuned by controlling its PZT. With the tuning of f_e, the optical frequency increases with time and presents a slope in Fig. 2(c). Meanwhile, f_b moves in the increasing and decreasing directions alternately, which is regarded as a triangular wave with a peak value of 50 MHz in Fig. 2(d). Once f_e is tuned to a sampling value, a feedback loop is activated by comparing the current f_b with a preset locking value. Then, PZT is back and forth controlled to

prevent the current f_b drift away from the preset value. In the locking process, both f_e and f_b keep stable, which present as flat steps in Figs. 2(c) and 2(d).
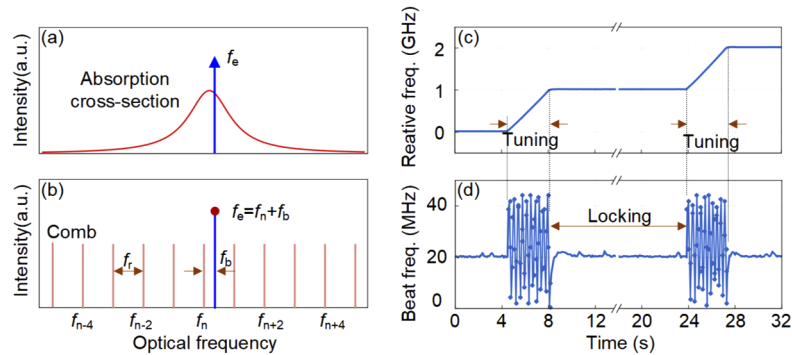

Fig. 2. The principle of frequency locking and tuning. (a) The frequency of seed laser f_e is scanned within the absorption cross-section of the gas. (b) The optical frequency f_e is precisely tracked by comb using heterodyne detection. (c) The optical frequency f_e changes over time when the frequency is locked and tuned. (d) The corresponding change of beat frequency f_b.

The PZT of the seed laser will go through a sudden stop from the tuning process to the locking process during the spectrum scanning. Under the circumstance, an optical frequency drift is introduced by the inertial position drift of the PZT. To evaluate the frequency stability of the locking technique, the beat frequency drift with and without locking are compared from the end of a tuning process, as shown in Figs. 3(a) and 3(b), respectively. The unlocking one presents a rapid drift of 150 MHz that the frequency is no longer the value expected. After rapid drift, the beat frequency begins to drift slowly over time by approximately 40 MHz. The overall drift during 120 s is nearly 190 MHz. As for the locking one, the preset locking value of the initial beat frequency is 25 MHz. Then, the beat frequency at this moment is fed and controlled immediately. By using the locking mechanism mentioned above, the frequency drift is restrained. In the whole measured period, the statistical of the locked beat frequency is centered at 25 MHz with a standard deviation of 0.5 MHz. For a pressure broadened absorption spectrum, the stability of the locked frequency can meet the spectrum scanning requirement [35].
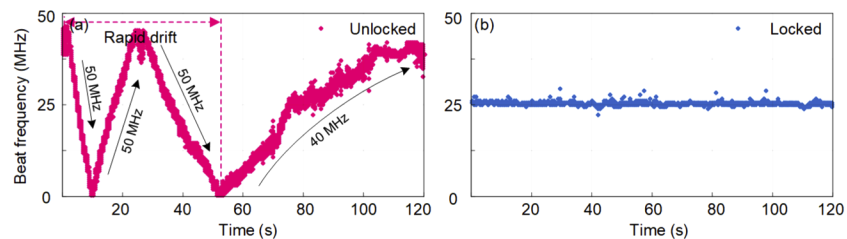

Fig. 3. The frequency stability versus time of (a) without and (b) with locking. The total drift without locking is approximately 200 MHz while the standard deviation of the locking one is 0.5 MHz centered at 25 MHz.

To evaluate the background and dark count rate, the raw backscatter signal in daytime and nighttime is shown in Fig. 4. The outgoing laser beam is pointed to a tall building at 6.4 km to block the laser, preventing the backscatter signal from overlapping with nearby pulses due to the pulse repetition of 20 kHz and ambiguous distance of 7.5 km. At daytime, the background noise is dominated by the solar radiation, whose count rate is over 30 kHz and depends on the

weather condition. At nighttime, the bandpass filter is removed to reduce the insertion loss. The background noise mainly involves the SNSPD dark noise and the radiation from the neon lights of the city, with a total count rate of about 1 kHz.
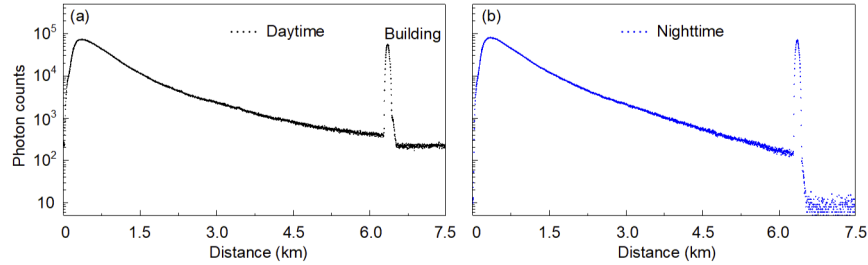

Fig. 4. The raw backscatter signals in (a) daytime and (b) nighttime.

The spectra scanning in the atmosphere with and without frequency locking technique was performed at 22:00 local time on October 9, 2020. The experiment was measured horizontally at an altitude of 50 m on the roof of a building. The sampling number is set as 30, which is sufficient to cover the entire spectrum and takes appropriate processing time. The frequency spacing is non-uniform for sampling more points at the high slope of the spectrum and improve the detection sensitivity [11,36]. Both sampling number and sampling spacing are programmable for different sampling requirements. The locking time at each frequency is 16 s and the scanning time per step is 4 s, leading to a time resolution of 10 min. Figure 5(a) shows one of the backscatter signals at a distance over 6 km when the emitted frequencies are scanned in succession. The main source of random noise is shot noise. As Poisson shot noise is presumed and dominated in the detection, the SNR at each wavelength can be evaluated by the root-mean-square of photon counts. The absorption coefficient at the center frequency is greater than that at the wings and the absorption depth increases versus distance. The optical depth spectrum can be extracted from the backscatter signal. The pulse width is 400 ns that corresponds to a 60 m range resolution. To improve the SNR, an average of 120 m is performed. Figures 5(b) and 5(c) represent two experiment results of the optical depth spectra at 4 km (differential optical depth spectra from 3.94 to 4.06 km) with a range resolution of 120 m and a time resolution of 10 min. It shows that the unlocked spectrum fluctuates obviously while the locked spectrum remains robust. In comparison, the measured spectrum without locking will gradually deviate from the actual line shape due to the free drift of sampling frequencies over the scanning process. By performing a Voigt fitting, the spectrum area fitting errors of the two are 2.3% and 1.3%, respectively. The precision of CO_2 concentration relating to the spectrum area fitting error (see Eq. (3)) is improved by applying the locking technique.

3.2. Spectrum analysis in different seasons

According to lidar equation, the range resolved optical depth at range R can be calculated as [18]

$$\alpha(R, f_i) = \ln\left[\frac{Q_i(R_1)Q_0(R_2)}{Q_0(R_1)Q_i(R_2)}\right], \tag{1}$$

where Q is the photon counts of lidar signal, subscript i indicates different frequencies, $Q0$ is chosen as the offline point with $\alpha(R, f_{30}) = 0$. R_1 and R_2 are two ranges before and after R, respectively. The range resolution is $\Delta R = R_2 - R_1$. The line shape of the optical depth can be
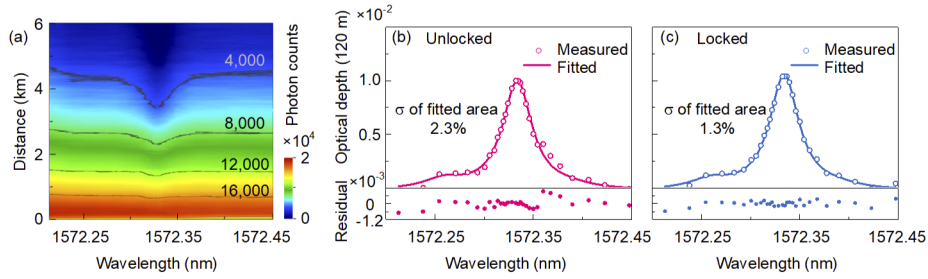
Fig. 5. (a) The raw backscatter signals of the scanning frequencies. Black lines: contour lines of photon counts. Each frequency is averaged for 16 s with a total scanning time of 10 min, optical depth (b) without and (c) with locking at 4 km (differential optical depth spectra from 3.94 to 4.06 km) with a range resolution of 120 m and a time resolution of 10 min. The experiment is carried out at 14:00 UTC (22:00 local time) on October 9, 2020 in autumn. The subfigures below (b) and (c) are residuals between the measured points and the fitted data, with the standard deviations of 3.5×10^{-4} and 2.1×10^{-4}, respectively. The scaling factors in optical depth and residual are $\times 10^{-2}$ and $\times 10^{-3}$, respectively.

represented as a Voigt function [37,38], which is expressed as

$$V(f) = A \frac{2\sqrt{ln2}y}{\omega_G \pi^{3/2}} \int_{-\infty}^{\infty} \frac{e^{-t^2}}{y^2 + (x-t)^2} dt, \tag{2}$$

where $x = (4 \ln 2)^{1/2}(f - f_0)/\omega_G$ and $y = (\ln 2)^{1/2}\omega_L/\omega_G$ are given for simplicity. A is the Voigt area, f_0 is the center frequency, ω_L is the Lorentzian full-width at half-maximum (FWHM), and ω_G is the Gaussian FWHM. ω_L and ω_G are broadened due to the molecular interaction, which can be determined by $\omega_L = 2P\gamma_0(T_0/T)^{n_{air}}$ and $\omega_G = f_0(8kT \ln 2/mc^2)^{1/2}$. Here, P is the gas pressure, γ_0 is the broadened Lorentzian half-width at half-maximum (HWHM) at 1 atm and $T_0 = 296$ K, and T is the measured temperature, n_{air} is the temperature exponent for the air-broadened HWHM, $k = 1.38 \times 10^{-23}$ J/K is Boltzmann constant, m is molecular mass, $c = 2.998 \times 10^8$ m/s is the speed of light.

Considering the mixture spectrum, a multi-peak Voigt fitting is performed [39]. The fitting model can be expressed as $V = b_0 + V_1 + V_2 + V_3 + \ldots$, where b_0 is the baseline, V_1, V_2, and V_3 are Voigt line functions for different gases from Eq. (2). By calculating the Lorentzian and Gaussian FWHM, and relative spacing of the center frequencies of these lines, the calculated optical depths $\alpha(R, f_i)$ are fitted to the multi-peak Voigt line model. Finally, the Voigt area and baseline can be retrieved. The area can also be expressed from Lambert-Beer's law as

$$A = S(T) \cdot N \cdot \Delta R. \tag{3}$$

In this expression, $S(T)$ is the line strength, N is the number density, ΔR is the length of a range cell. So that the concentration can be calculated from N using the ideal-gas equation.

The R16 line of CO_2 has been widely used for atmospheric CO_2 measurement due to its high absorption strength and low temperature sensitivity. Table 2 illustrates the spectroscopic parameters of several gases located in the scanning range of 1572.2 - 1572.45 nm. It shows that this R16 line mainly contains the absorption of three gases, namely CO_2, H_2O, and HDO. The line intensity S_0 in Table 2 is obtained from HITRAN 2016 [40], with its value multiplied by natural abundance. However, when considering the interaction of three gases, the value of S_0 should be corrected to S_0' according to natural abundance. After the correction, the S_0' of H_2O is five orders of magnitude lower than that of CO_2 so that the interference can be almost neglected. But the line intensity of two HDO lines possess nearly the same order of magnitude with CO_2, thus the interfering should be further discussed.

Table 2. Spectroscopic parameters of several interfering gases from HITRAN 2016.[a]

Formula	v	Abund.	S_0	S_0'	γ_{air}	γ_{self}	E''	n_{air}
$HD^{16}O$	6359.7477	0.000311	2.218×10^{-26}	7.139×10^{-23}	0.0885	0.41	362.507	0.63
$^{12}C^{16}O_2$	6359.9672	0.984204	1.779×10^{-23}	1.808×10^{-23}	0.0747	0.102	106.130	0.67
$H_2^{16}O$	6360.0255	0.997317	3.547×10^{-28}	3.557×10^{-28}	0.0554	0.235	2551.482	0.4
$HD^{16}O$	6360.2783	0.000311	8.619×10^{-26}	2.774×10^{-22}	0.0995	0.398	100.391	0.71

[a]v (cm^{-1}): wavenumber; Abund.: natural abundance; S (cm^{-1}/(molec·cm^{-2})): line intensity, multiplied by isotopologue abundance at 296 K; S' (cm^{-1}/(molec·cm^{-2})): corrected line intensity; γ_{air} (cm^{-1}·atm^{-1}): air-broadened Lorentzian half-width at half-maximum (HWHM) at 1 atm and 296 K; γ_{self} (cm^{-1}·atm^{-1}): self-broadened HWHM at 1 atm pressure and 296 K; E'' (cm^{-1}): lower state energy; n_{air}: temperature exponent for the air-broadened HWHM.

The mixture spectra of CO_2 and HDO in two different atmospheric environments are simulated according to the Eq. (2) and the spectroscopic parameters in Table 2. One case is for relatively low absolute humidity of dry air while the other case is the reverse for moist air (H_2O: 4 g/m^3, CO_2: 400 ppm for case 1 and H_2O: 16 g/m^3, CO_2: 400 ppm for case 2). Figure 6 presents two simulated mixture models with a temperature of 296 K and a pressure of 1 atm. The models show that the mixture spectra are the superposition of three absorption lines. Under the circumstances, the line intensity of CO_2 is approximately 17 and 4.25 times stronger than that of HDO, respectively, with a deeper absorption depth in Fig. 6(b) than in Fig. 6(a). Thus different concentrations of HDO have different influences on the mixture absorption, which can roughly correspond to different seasons. Namely, the HDO mass per unit volume becomes less in winter with a minuscule effect on CO_2 measurement while a high content of HDO in summer presents a more obvious interaction.
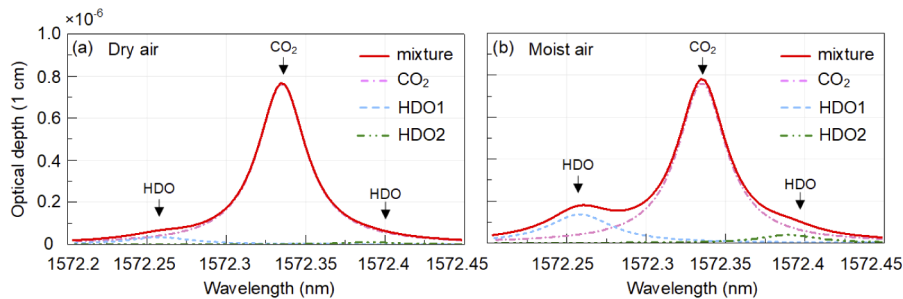

Fig. 6. The absorption optical depth per centimeter of gas mixtures model in (a) dry air (H_2O: 4 g/m^3, CO_2: 400 ppm) and (b) moist air (H_2O: 16 g/m^3, CO_2: 400 ppm). The red line: the mixture gas model superimposed by two weak HDO lines and a strong CO_2 line.

The spectra in different seasons are investigated to experimentally analyze the influence of HDO on independent CO_2 spectrum measurement. The experiments were performed on January 3, 2020 for the winter case and August 19, 2020 for the summer case, with the same sampling number and the spacing as Fig. 5. The absolute humidity of the two measurements are close to 3 g/m^3 and 20 g/m^3 for winter and summer measurements, provided by an in-situ sensor (Vaisala windcap WMT52). Figure 7 shows the measured optical depth spectra in two cases at 4 km with a range resolution of 120 m, respectively. Both results are consistent with the theoretical model. By applying a three-peak Voigt fitting, the CO_2 line and HDO lines can be separated. Here, the two HDO lines are fitted with a fixed ratio of the two peaks. In winter, the fitted CO_2 line is close to the mixture line in Fig. 7(a), thus the R16 line of CO_2 can be considered as minimal interference for CO_2 measurement. While in summer, the relatively high absorption of two HDO lines is shown in Fig. 7(b), with a non-negligible influence of HDO.
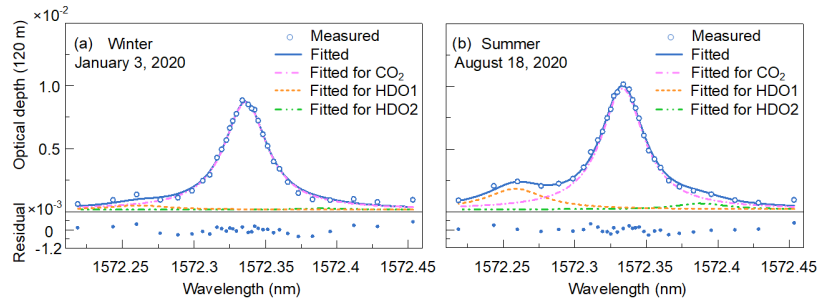
Fig. 7. Measured optical depth at 4 km with a range resolution of 120 m (differential optical depth spectra at 3.94 and 4.06 km) and a time resolution of 10 min (a) in winter, 13:00 UTC on January 3, 2020, with the absolute humidity of 3 g/m^3, and (b) in summer, 13:00 UTC on August 18, 2020, with the absolute humidity of 20 g/m^3. The subfigures below (a) and (b) are fit residuals. The blue circle: the measured results with 30 scanning frequencies; The blue line: the fitted mixture line with the Voigt model; The light magenta dot-dash line: independent CO_2 line. The scaling factors in optical depth and residual are $\times 10^{-2}$ and $\times 10^{-3}$, respectively.

Figure 8 shows the measured concentrations of CO_2 and HDO from September 25 to September 26, 2020 over 6 km. For comparison purposes, gas concentrations from in-situ sensors are also plotted. In the experiment, two in-situ sensors (Thermo Scientific 410i and Vaisala windcap WMT52) were placed at 4 km in the optical path for CO_2 and H_2O measurements, respectively. The concentration of H_2O is converted into HDO by using the relative natural abundance in Table 2. The retrieved concentrations from lidar are based on the differential optical depth spectra from 3.94 to 4.06 km with time resolutions of 10 min and 30 min for CO_2 and HDO, respectively. And the comparisons of the retrievals and in-situ sensors measurements vs. time in Figs. 8(a) and
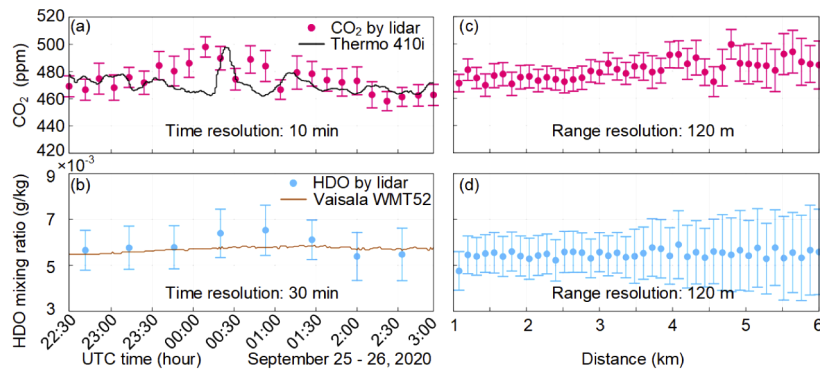

Fig. 8. (a) Comparison of the CO_2 retrieval from lidar and the in-situ sensor measurements at 4 km (3.94 ~ 4.06 km) vs. time from 22:30 UTC on September 25, 2020 to 03:00 UTC on September 26, 2020 with range and time resolution of 120 m and 10 min, respectively, (b) Comparison of the HDO dry air mixing ratios retrieval from lidar and Vaisala WMT52 measurements at 4 km vs. time with a time resolution of 30 min. Time on the abscissa is UTC (local time −8 hrs), (c) The CO_2 retrieval from lidar measurement at 00:45 UTC vs detection distance with a range resolution of 120 m, (d) The HDO retrieval from lidar measurement at 02:00 UTC vs detection distance. The error bars are ±1 standard deviation.

8(b) show agreement. The standard deviations between comparisons are 11.1 μmol/mol (ppm) and 0.4×10^{-3} g/kg for CO_2 and HDO, respectively. Figures 8(c) and 8(d) show concentrations of CO_2 and HDO along the optical path at 00:45 UTC over 6 km with a range resolution of 120 m. The measurement precisions are 6.5 μmol/mol (ppm) and 1×10^{-3} g/kg for CO_2 and HDO which are near 1.5% and 15% of the ambient levels, respectively. The low precision of HDO is due to its weak absorption and sparse sampling data.

4. Conclusion

We have demonstrated a wide-band gas analysis lidar incorporating a comb-referenced scanning laser for CO_2 spectrum scanning. The locking performance is evaluated, which effectively restrains the frequency drift of the laser with an uncertainty of 0.5 MHz. The atmospheric CO_2 spectrum scanning experiment is carried out with a range resolution of 120 m and a time resolution of 10 min. The interactions of CO_2 and HDO are investigated by measuring the R16 line of CO_2 in winter and summer, which is further corrected by triple-peak Voigt fitting. The concentration of CO_2 and HDO are retrieved with a measurement precision of 1.5% for CO_2 and 15% for HDO. Future studies of the improved system can be adapted to measurements of other gases, such as H_2O, NH_3, H_2S, etc., whose absorption spectrum locates in the range of the tunable laser and the frequency comb. The promising applications of the system involve isotopic ratio measurement, gas monitoring, leakage warning and atmospheric composition, and plume emission of stacks.

Note that the atmospheric turbulence is usually an issue in measurement over long horizontal path, which degrades the spatial coherence of the propagating beam and affects the coupling efficiency of telescope from space to the fiber [41]. Here, the turbulence effect is suppressed by using the SNSPD with large active diameter of 50 μm [42,43]. In the near future, we plan to add a reference laser at offline wavelength using time-domain-multiplexing technique, emitting alternatively with the probe laser to compensate the signal fluctuation due to turbulence.

Disclosures. The authors declare that there are no conflicts of interest related to this article.

Data availability. Data underlying the results presented in this paper can be obtained from the authors upon reasonable request.

References

1. B. Fu, T. Gasser, B. Li, B. S. Tao, P. Ciais, S. Piao, Y. Balkanski, W. Li, T. Yin, L. Han, X. Li, Y. Han, J. An, S. Peng, and J. Xu, "Short-lived climate forcers have long-term climate impacts via the carbon-climate feedback," Nat. Clim. Chang. **10**(9), 851–855 (2020).
2. T. R. Karl and K. E. Trenberth, "Modern global climate change," Science **302**(5651), 1719–1723 (2003).
3. S. Solomon, M. Manning, M. Marquis, and D. Qin, "*Climate change 2007-the physical science basis: Working group I contribution to the fourth assessment report of the IPCC*," (Vol. 4), Cambridge University (2007).
4. J. M. Hartmann, H. Tran, and G. C. Toon, "Influence of line mixing on the retrievals of atmospheric CO_2 from spectra in the 1.6 and 2.1 μm regions," Atmos. Chem. Phys. Discuss. **9**(1), 4873–4898 (2009).
5. C. Le Quéré, M. R. Raupach, J. G. Canadell, G. Marland, L. Bopp, P. Ciais, T. J. Conway, S. C. Doney, R. A. Feely, P. Foster, P. Friedlingstein, K. Gurney, R. A. Houghton, J. I. House, C. Huntingford, P. E. Levy, M. R. Lomas, J. Majkut, N. Metzl, J. P. Ometto, G. P. Peters, I. C. Prentice, J. T. Randerson, S. W. Running, J. L. Sarmiento, U. Schuster, S. Sitch, T. Takahashi, N. Viovy, G. R. Werf, and F. Woodward, "Trends in the sources and sinks of carbon dioxide," Nat. Geosci. **2**(12), 831–836 (2009).
6. D. W. T. Griffith, R. Leuning, O. T. Denmead, and I. M. Jamie, "Airland exchanges of CO_2, CH_4 and N_2O measured by FTIR spectrometry and micrometeorological techniques," Atmos. Environ. **36**(11), 1833–1842 (2002).
7. C. Clerbaux, A. Boynard, L. Clarisse, M. George, J. Hadji-Lazaro, H. Herbin, D. J. Hurtmans, M. Pommier, A. Razavi, S. Turquety, C. Wespes, and P. F. Coheur, "Monitoring of atmospheric composition using the thermal infrared IASI/MetOp sounder," Atmos. Chem. Phys. **9**(16), 6041–6054 (2009).
8. M. Queißer, M. Burton, and R. Kazahaya, "Insights into geological processes with CO_2 remote sensing–A review of technology and applications," Earth-Sci. Rev. **188**, 389–426 (2019).
9. A. Amediek, G. Ehret, A. Fix, M. Wirth, C. Büdenbender, M. Quatrevalet, C. Kiemle, and C. Gerbig, "CHARM-F—a new airborne integrated-path differential-absorption lidar for carbon dioxide and methane observations: measurement performance and quantification of strong point source emissions," Appl. Opt. **56**(18), 5182–5197 (2017).

10. N. Cezard, S. Le Mehaute, J. Le Gouët, M. Valla, D. Goular, D. Fleury, P. Christophe, and A. Dolfi-Bouteyre, "Performance assessment of a coherent DIAL-Doppler fiber lidar at 1645 nm for remote sensing of methane and wind," Opt. Express **28**(15), 22345–22357 (2020).

11. J. B. Abshire, A. K. Ramanathan, H. Riris, G. R. Allan, X. Sun, W. E. Hasselbrack, J. Mao, S. Wu, J. Chen, K. Numata, S. R. Kawa, M. Ying, M. Yang, and J. D. Gangi, "Airborne measurements of CO_2 column concentrations made with a pulsed IPDA lidar using a multiple-wavelength-locked laser and HgCdTe APD detector," Atmos. Meas. Tech. **11**(4), 2001–2025 (2018).

12. S. R. Kawa, J. B. Abshire, D. F. Baker, E. V. Browell, D. Crisp, S. M. Crowell, J. J. Hyon, J. C. Jacob, K. W. Jucks, B. Lin, R. T. Menzies, L. E. Ott, and T. S. Zaccheo, *Active Sensing of CO_2 Emissions over Nights, Days, and Seasons (ASCENDS): Final Report of the ASCENDS Ad Hoc Science Definition Team*," NASA Technical Report, NASA/TP–2018-219034, (2018).

13. J. Caron, Y. Durand, J. Bezy, and R. Meynart, "Performance modeling for ASCOPE: a space-borne lidar measuring atmospheric CO_2," Proc. SPIE **7479**, 74790E (2009).

14. C. Kiemle, M. Quatrevalet, G. Ehret, A. Amediek, A. Fix, and M. Wirth, "Sensitivity studies for a space-based methane lidar mission," Atmos. Meas. Tech. **4**(10), 2195–2211 (2011).

15. G. Ehret, P. Bousquet, C. Pierangelo, M. Alpers, B. Millet, J. B. Abshire, H. Bovensmann, J. P. Burrows, F. Chevallier, P. Ciais, C. Crevoisier, A. Fix, P. Flamant, C. Frankenberg, F. Gibert, B. Heim, M. Heimann, S. Houweling, H. W. Hubberten, P. Jöckel, K. Law, A. Löw, J. Marshall, A. A. Panareda, S. Payan, C. Prigent, P. Rairoux, T. Sachs, M. Scholze, and M. Wirth, "MERLIN: A French-German space lidar mission dedicated to atmospheric methane," Remote Sens. **9**(10), 1052 (2017).

16. K. Numata, J. R. Chen, S. T. Wu, J. B. Abshire, and M. A. Krainak, "Frequency stabilization of distributed-feedback laser diodes at 1572 nm for lidar measurements of atmospheric carbon dioxide," Appl. Opt. **50**(7), 1047–1056 (2011).

17. K. Numata, J. R. Chen, and S. T. Wu, "Precision and fast wavelength tuning of a dynamically phase-locked widely-tunable laser," Opt. Express **20**(13), 14234–14243 (2012).

18. G. A. Wagner and D. F. Plusquellic, "Multi-frequency differential absorption LIDAR system for remote sensing of CO_2 and H_2O near 1.6 μm," Opt. Express **26**(15), 19420–19434 (2018).

19. M. Queisser, M. Burton, G. R. Allan, and A. Chiarugi, "Portable laser spectrometer for airborne and ground-based remote sensing of geological CO_2 emissions," Opt. Lett. **42**(14), 2782–2785 (2017).

20. B. R. Washburn, R. W. Fox, N. R. Newbury, J. W. Nicholson, K. Feder, P. S. Westbrook, and C. G. Jørgensen, "Fiber-laser-based frequency comb with a tunable repetition rate," Opt. Express **12**(20), 4999–5004 (2004).

21. S. T. Cundiff and J. Ye, "Colloquium: Femtosecond optical frequency combs," Rev. Mod. Phys. **75**(1), 325–342 (2003).

22. G. W. Truong, E. M. Waxman, K. C. Cossel, E. Baumann, A. Klose, F. R. Giorgetta, W. C. Swann, N. R. Newbury, and I. Coddington, "Accurate frequency referencing for fieldable dual-comb spectroscopy," Opt. Express **24**(26), 30495–30504 (2016).

23. G. B. Rieker, F. R. Giorgetta, W. C. Swann, J. Kofler, A. M. Zolot, L. C. Sinclair, E. Baumann, C. Cromer, G. Petron, C. Sweeney, P. P. Tans, I. Coddington, and N. R. Newbury, "Frequency-comb-based remote sensing of greenhouse gases over kilometer air paths," Optica **1**(5), 290–298 (2014).

24. I. R. Coddington, N. R. Newbury, and W. C. Swann, "Dual-comb spectroscopy," Optica **3**(4), 414–426 (2016).

25. K. C. Cossel, E. M. Waxman, F. R. Giorgetta, M. Cermak, I. R. Coddington, D. Hesselius, S. Ruben, W. C. Swann, G. W. Truong, G. B. Rieker, and N. R. Newbury, "Open-path dual-comb spectroscopy to an airborne retroreflector," Optica **4**(7), 724–728 (2017).

26. V. Ahtee, M. Merimaa, and K. Nyholm, "Precision spectroscopy of acetylene transitions using an optical frequency synthesizer," Opt. Lett. **34**(17), 2619–2621 (2009).

27. S. E. Park, E. B. Kim, Y.-H. Park, D. S. Yee, T. Y. Kwon, and C. Y. Park, "Sweep optical frequency synthesizer with a distributed-Braggreflector laser injection locked by a single component of an optical frequency comb," Opt. Lett. **31**(24), 3594–3596 (2006).

28. D. J. Jones, S. A. Diddams, J. K. Ranka, A. Stentz, R. S. Windeler, J. L. Hall, and S. T. Cundiff, "Carrier-envelope phase control of femtosecond mode-locked lasers and direct optical frequency synthesis," Science **288**(5466), 635–639 (2000).

29. M. Shangguan, H. Xia, C. Wang, J. Qiu, S. Lin, X. Dou, Q. Zhang, and J. W. Pan, "Dual-frequency Doppler lidar for wind detection with a superconducting nanowire single-photon detector," Opt. Lett. **42**(18), 3541–3544 (2017).

30. S. Miki, M. Yabuno, T. Yamashita, and H. Terai, "Stable, high-performance operation of a fiber-coupled superconducting nanowire avalanche photon detector," Opt. Express **25**(6), 6796–6804 (2017).

31. C. Zhang, W. Zhang, L. You, J. Huang, H. Li, X. Sun, H. Wang, C. Lv, H. Zhou, X. Liu, Z. Wang, and X. Xie, "Suppressing dark counts of multimode-fiber-coupled superconducting nanowire single-photon detector," IEEE Photonics J. **11**(5), 1–8 (2019).

32. G. N. Gol'tsman, A. Korneev, I. Rubtsova, I. Milostnaya, G. Chulkova, O. Minaeva, K. Smirnov, B. Voronov, W. Słysz, A. Pearlman, A. Verevkin, and R. Sobolewski, "Ultrafast superconducting single-photon detectors for near-infrared-wavelength quantum communications," phys. stat. sol. (c) **2**(5), 1480–1488 (2005).

33. E. Cadiou, D. Mammez, J. B. Dherbecourt, G. Gorju, J. Pelon, J. M. Melkonian, A. Godard, and M. Raybaut, "Atmospheric boundary layer CO_2 remote sensing with a direct detection LIDAR instrument based on a widely tunable optical parametric source," Opt. Lett. **42**(20), 4044–4047 (2017).

34. X. Sun, J. B. Abshire, J. D. Beck, P. Mitra, K. Reiff, and G. Yang, "HgCdTe avalanche photodiode detectors for airborne and spaceborne lidar at infrared wavelengths," Opt. Express **25**(14), 16589–16602 (2017).

35. G. R. Allan, H. Riris, J. B. Abshire, X. Sun, E. Wilson, J. F. Burris, and M. A. Krainak, "Laser sounder for active remote sensing measurements of CO_2 concentrations," *IEEE Aerosp. Conf.* 1–7. IEEE (2008).

36. G. Han, H. Xu, W. Gong, X. Ma, and A. Liang, "Simulations of a multi-wavelength differential absorption lidar method for CO_2 measurement," Appl. Opt. **56**(30), 8532–8540 (2017).

37. T. Ida, M. Ando, and H. Toraya, "Extended pseudo-Voigt function for approximating the Voigt profile," J. Appl. Crystallogr. **33**(6), 1311–1316 (2000).

38. B. H. Armstrong, "Spectrum line profiles: the Voigt function," J. Quant. Spectrosc. Radiat. Transfer **7**(1), 61–88 (1967).

39. J. Guezenoc, V. Payré, C. Fabre, D. Syvilay, A. Cousin, A. Gallet-Budynek, and B. Bousquet, "Variable selection in laser-induced breakdown spectroscopy assisted by multivariate analysis: An alternative to multi-peak fitting," Spectrochim. Acta, Part B **152**, 6–13 (2019).

40. I. E. Gordon, L. S. Rothman, C. Hill, R. V. Kochanov, Y. Tan, P. F. Bernath, M. Birk, V. Boudon, A. Campargue, K. V. Chance, B. J. Drouin, J. M. Flaud, R. R. Gamache, J. T. Hodges, D. Jacquemart, V. I. Perevalov, A. Perrin, K. P. Shine, M. A. H. Smith, J. Tennyson, G. C. Toon, H. Tran, V. G. Tyuterev, A. Barbe, A. G. Császár, V. M. Devi, T. Furtenbacher, J. J. Harrison, J. M. Hartmann, A. Jolly, T. J. Johnson, T. Karman, I. Kleiner, A. A. Kyuberis, J. Loos, O. M. Lyulin, S. T. Massie, S. N. Mikhailenko, N. Moazzen-Ahmadi, H. S. P. Müller, O. V. Naumenko, A. V. Nikitin, O. L. Polyansky, M. Rey, M. Rotger, S. W. Sharpe, K. Sung, E. Starikova, S. A. Tashkun, J. V. Auwera, G. Wagner, J. Wilzewski, P. Wcisło, S. Yu, and E. J. Zak, "The hitran 2016 molecular spectroscopic database," J. Quant. Spectrosc. Radiat. Transfer **203**, 3–69 (2017).

41. Y. Dikmelik and F. M. Davidson, "Fiber-coupling efficiency for free-space optical communication through atmospheric turbulence," Appl. Opt. **44**(23), 4946–4952 (2005).

42. S. Arisa, Y. Takayama, H. Endo, R. Shimizu, M. Fujiwara, and M. Sasaki, "Coupling efficiency of laser beam to multimode fiber for free space optical communication," Proc. SPIE **274**(2), 315–319 (2007).

43. D. Zheng, Y. Li, E. Chen, B. Li, D. Kong, W. Li, and J. Wu, "Free-space to few-mode-fiber coupling under atmospheric turbulence," Opt. Express **24**(16), 18739–18744 (2016).